Meteorol. Z. (Contrib. Atm. Sci.), Vol. **29**, No. 6, 439–449 (published online July 17, 2020)

Miniature high-frequency chilled-mirror hygrometer for atmospheric measurements aboard fixed wing UAS

Moritz Mauz[1*], Bram van Kesteren[1], Wolfgang Junkermann[2], Kjell zum Berge[1], Martin Schön[1], Andreas Platis[1] and Jens Bange[1]

[1]Centre for Applied Geoscience, University of Tübingen, Germany
[2]Institute for Meteorology and Climate Research, Karlsruhe Institute of Technology, Garmisch-Partenkirchen, Germany

(Manuscript received January 2, 2020; in revised form April 30, 2020; accepted April 30, 2020)

Abstract

A small light-weight in-house made miniature chilled-mirror hygrometer (CMH) for fixed wing UAS (unmanned aircraft system) is presented, with its features and limitations. Therefore, first measurements of the CMH equipped on the small research UAS of type MASC-3 (multi-purpose airborne sensor carrier) operated by the University of Tübingen are shown. A comparison against a very accurate state of the art capacitive industrial humidity sensor (SHT31) is done. The sensor consists of a TEC (thermoelectric cooler) covered by a gold mirror. The TEC is controlled by a commercially available microprocessor with an on-board PID (proportional-integral-derivative) controller. The results of the CMH measurements are in good agreement with the industrial-made capacitive sensor. The absolute accuracy of the measured dew point temperature by the CMH is in the range of ±0.2 K. Spectra show evidence that the CMH is capable to measure turbulent humidity fluctuations in the atmosphere with a temporal resolution of up to 10 Hz. Such a fast humidity sensor aboard a small UAS has the potential to study humidity fluxes in the surface layer over complex terrain, behind wind energy converters and humidity variations over land and sea surfaces in general.

Keywords: Chilled mirror hygrometer, Unmanned Aircraft System, high frequency humidity measurement, Boundary Layer Measurements

1 Introduction

Together with temperature, pressure, and the 3D wind vector, water vapour is a key parameter to describe the state of the atmosphere. Water vapour is the most important greenhouse gas on Earth and plays an important role in energy transfer through the atmosphere because of its heat capacity. Furthermore, evapotranspiration of water at the surface contributes substantially to the energy budget at the Earth surface, due to the high enthalpy of evaporation. Because of its low molar mass, moisture increases the buoyancy of air and thus affects atmospheric stability, especially over sea surfaces and vegetated soils (Koufang Lo, 1996; Stull, 2000). The water vapour transport into the atmosphere is essentially turbulent; and as such, water vapor fluxes are one of the key observational parameters in established monitoring networks like FLUXNET (Baldocchi et al., 2001), TERENO (Bogena et al., 2015), ICOS (Rebmann et al., 2018) and NEON (neonscience.org, 2019) and several large field campaigns in complex terrain, e.g. Scalex (Wolf et al., 2017) and LITFASS (Beyrich et al., 2002b; Beyrich et al., 2002a; Beyrich et al., 2006).

Fast-response humidity sensors that can capture the relevant turbulence time-scales are open- or closed-path optical absorption techniques, such as Lyman alpha, TDL (tunable diode laser) or IR (infrared) absorption. These sensors can accurately determine the variance, the structure parameter, or other relevant turbulent humidity parameters (De Bruin et al., 1993). In combination with fast-response anemometers, these point-source measurements additionally allow for accurate estimates of the humidity flux on times scales of 15–30 min (Shuttleworth, 2007). In combination with laser scintillometers, sampling time of humidity fluxes can be reduced to 1 min under homogeneous conditions (Van Kesteren et al., 2013a; Van Kesteren et al., 2013b). However, the above presented methods are impossible to implement on mobile platforms and only represent small geographic areas, which especially in heterogeneous conditions limits their applicability as a reference in e.g. numerical models or water-balance estimates (Foken, 2008). Microwave scintillometers allow for determining the structure parameter of humidity, or in combination with a large aperture scintillometer also fluxes, under heterogeneous conditions over scales of up to 10 km (Meijninger et al., 2006; Ward et al., 2015a; Ward et al., 2015b). But scintillometers only provide an average quantity over the length of the measurement path.

Alternatively, Lyman-alpha and infrared absorption hygrometers can be installed on helipod (pod of me-

*Corresponding author: Moritz Mauz, Centre for Applied Geoscience, University of Tübingen, Hölderlinstr. 12, 72074 Tübingen, Germany, e-mail: moritz.mauz@uni-tuebingen.de

DOI 10.1127/metz/2020/1026

teorological equipment dragged by a helicopter) or manned aircraft to obtain spatial information on the turbulent exchange of humidity, e.g. (Platis et al., 2017; Lampert et al., 2018; Bange and Roth, 1999; Muschinski et al., 2001). However, these airborne systems are expensive and limited in their mobility by aviation laws. Manned aircraft are typically restricted to flight altitudes of approximately 150 m above ground, and special permissions are required for lower flight altitudes. In some occasions lower altitudes down to 25 m have been reported using small environmental research aircraft (SERAs) (Metzger et al., 2011; Neininger and Hacker, 2012). Recent technical developments in drone technique led to an increased application of cheap, light-weight unmanned aerial systems (Spiess et al., 2007; van den Kroonenberg et al., 2012; Rautenberg et al., 2019). However, so far suitable fast response-humidity sensors have not been available.

For (small) unmanned aircraft systems (UAS), the weight of a measuring instrument is an important factor. Instruments that work well on a manned aircraft or helipods typically weigh more than 2 kg, which exceeds the payload for these small aircraft. Low weight capacitive moisture sensors, which are typically installed on meteorological towers (Kuner et al., 2015), are light enough; but their response time is smaller than 1 Hz. As such, these sensors are not fast enough to capture the relevant turbulent scales. Wildmann et al. (2014a) attempted to increase the response time of a capacitive sensor by post-processing the humidity data, while implying an inverse model. This method allows to obtain humidity data up to 3 Hz. However, despite careful calibration, data accuracy suffers because of an increased noise level, which in practice makes the method unsuitable.

An alternative to capacitive sensors are lightweigth dew point mirrors or chilled-mirror hygrometers (CMHs). Their measurement principle is based on cooling the surface of a small mirror until condensation occurs, while monitoring its temperature. With a properly designed feedback system, the mirror is maintained at the temperature at which the rate of condensation equals the rate of dew evaporation. In this state, the condensed water is in equilibrium with the water vapour pressure of the surrounding air, thus defining the dew point temperature (Stull, 2000). This kind of dew point sensors are applied in radiosondes, where they measure moisture with a measurement frequency of up to 1 Hz (Vömel et al., 2003). Comparison and evaluation of a commercial chilled-mirror hygrometer to a capacitive sensor (Humicap) show that this type of sensor performs well, even for the challenging radiosonde application (Fujiwara et al., 2003). Unfortunately, commercial sensors still lack the temporal resolution required for accurate turbulent humidity measurements.

In this work, an approach for doing accurate high-frequency measurements of water vapour is presented that can capture the smallest turbulent time scales. The goal of such a sensor is to be able to study the underlying processes related to water vapour fluctuations and water vapour transport in the lower atmosphere. To this end, a small chilled-mirror hygrometer is tuned to allow for a high-frequency output and mounted it on a small UAS, the MASC-3, that operates in the lower parts of the atmospheric boundary layer (in this study up to about 200 m) (Rautenberg et al., 2019). The hygrometer performance is compared against capacitive humidity sensors mounted on a meteorological observation tower and a capacitive sensor mounted on the UAS. As we will show, our tuned hygrometer provides a high measurement frequency (>5 Hz) with a minimal need of maintenance.

2 Setting-up the chilled-mirror hygrometer

A chilled-mirror hygrometer (CMH) measures the dew point temperature of the air that ventilates it. By cooling the polished metallic surface of the mirror, water condenses on its surface and this dew causes a strong signal change on the luminosity sensor that monitors the brightness of the mirror. Consequently, the crucial parts are: a temperature sensor, a thermoelectric cooler (TEC) controller that regulates the temperature of the surface that is measured and a high frequency luminosity sensor. The heat capacity of the golden mirror is also a critical parameter. Of course, the heat capacity of the golden mirror can be calculated and the mirror should be as thin as possible, yet, this delaying parameter is only available implicitly. To circumvent this problem, only small currents are applied to the TEC, so that an equilibrium between the inflow of the air that reheats the mirror and the current that cools the mirror, is achieved.

Our humidity sensor is made from commercially available parts (cf. Table 1). Figure 1 shows a schematic of the hygrometer and its components. Basically, a light-sensitive diode (the luminosity sensor) measures the reflection of light emitted by a light-emitting diode (LED) from the mirror. Increasing dew accumulation on the mirror decreases the direct reflection into the luminosity sensor, whereas the amount of diffusely scattered light is increased. The proportional-integral-derivative (PID) controller regulates the voltage output to the TEC (values between 0–4.5 V), ensuring a constant reflected light level. In default mode the TEC surface is actively cooled, whereas the thermal energy of the inflowing air is used to heat the mirror. In our airborne application, ventilation is achieved by using the dynamic air pressure at the inlet (ram air), channelled to the measurement chamber onto the TEC reflective surface. At a typical true air speed of 18.5 m s^{-1} (speed relative to the air), a calculated volumetric flow of $\approx 0.27\,\mathrm{l\,min^{-1}}$ is achieved through the inlet (aperture 0.25 mm^2).

2.1 Specifications

The Arduino Nano has a CPU (central processing unit) clocking speed of 16 MHz. This is enough to provide

Table 1: Various parts of the in-house built CMH. * Component from a Snow White® CMH from Meteolabor AG

Function	Component
Light source	white LED
Luminosity sensor	Adafruit TSL2561
Temperature measurement	TC type T *
Temperature read-out	Adafruit MAX31856
Microcontroller	Arduino Nano
Thermo-electric cooling	≈2.5 W *

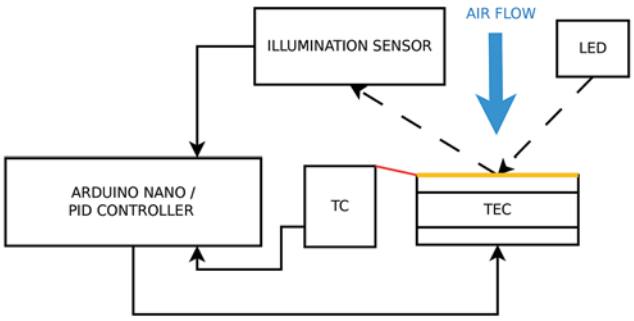

Figure 1: Schematic of the CMH mode of operation. The CMH consists of commercially available parts, e.g. the microprocessor (Arduino Nano) that, among other routines, hosts the PID controller that regulates the voltage output to the thermoelectric cooler (TEC). The golden layer on the TEC is the mirror that is in direct contact with the inflowing air. The thermocouple (TC) thermometer measures the mirror temperature.

a logging speed of 52 Hz, causing one measurement cycle to be about 19 ms long. Consequently, the integration time for the PID controller is also 19 ms. The temperature measurement (TC) is sensor-wise digitally limited to roughly 12 Hz, which correspondingly is the theoretical maximum attainable output-frequency of our hygrometer.

The light source of the sensor is a white LED supplied with a constant voltage stabilised by a Z-diode. The PID controller is set to hold a fixed illumination which is equivalent to the dew point criterion on the TEC surface. For this prototype, the target illumination is 1150 lux. An advantage of the PID controller is that the voltage sent to the TEC to cool the mirror is not only proportional to the illumination signal, but also takes into account an integral term that is proportional to both the magnitude of the error and the duration of the error (time the signal is off the set-point) as well as the derivative representing the past rate of cooling.

Here, the error is the deviation of the current illumination level from the target value (also called the set point). This kind of cooling regulation minimises overmodulation or forced oscillations that result from operation of on/off controllers or simple P (proportional) controllers (Narvekar and Upadhye, 2016). A PID controller is recommended when dealing with higher order capacitive processes (Rao and Mishra, 2014).

A long-term drift, as in open-path humidity sensors (Mammarella et al., 2009), does not occur in chilled-mirror humidity sensors. Also LED ageing (fading) is not a concern. Typically LEDs fade to a value of 98 % of their initial luminosity after 2000–6000 operating hours. Similar values can be assumed for the illumination detection diode. However, a potential source of error is contamination of the mirror surface by any pollutant transported in the air that may condense or adhere to it. Regular inspection and cleaning of the surface, when polluted, e.g. by pollen, will prevent erroneous measurements. Furthermore, due to the high performance of the TEC, an appropriate heat sink is required. In our airborne application, the heat sink is exposed to the air flow along the fuselage of the UAS, providing sufficient heat release.

2.2 Calibration of the CMH

A dew point sensor does not need a calibration like for example a resistance thermometer (e.g. five point calibration). However, for each sensor it is necessary to define a dew point criterion, i.e. target illumination for the illumination sensor. This target illumination was found by operating the chilled-mirror hygrometer next to the SHT31 sensor in a small wind tunnel. The wind tunnel provides a steady stream of air, with laminar flow at a constant humidity. Correct tuning of the target illumination is achieved when the dew point measurement of the chilled-mirror hygrometer matches that of the SHT31. This procedure does not assure absolute accuracy of the chilled-mirror sensor, but provides a good estimate for the necessary target illumination.

A small offset between both sensors has been found to yield the fastest response time for our sensor. This bias corresponds to an undercut of the target illumination. Undercutting the illumination helps stabilising the PID controller, i.e. minimising over-regulation, by providing a stable layer of dew on the mirror.

3 Measurement system and measurement site for data comparison

3.1 Research UAS

The research UAS MASC-3 (multi-purpose airborne sensor carrier) (see Figure 2 and Table 2) is a fixed wing airborne measurement system designed and operated by the University of Tübingen (Wildmann et al., 2013; Wildmann et al., 2014b; Wildmann et al., 2014a; Wildmann et al., 2014c). Depending on payload and batteries, it has a take-off weight between 5 and 8 kg and the UAS has an endurance between 1.5 and 2 hours. To reduce disturbance introduced by the air of the MASC-3's propeller and engine; a pusher configuration was selected, i.e. the propulsion system is located at the back of the aircraft. For automatic

Figure 2: MASC-3 UAS shortly after take-off. The winch cable is still attached to the fuselage. Photo taken at the ISOBAR campaign 2018, courtesy Astrid Lampert

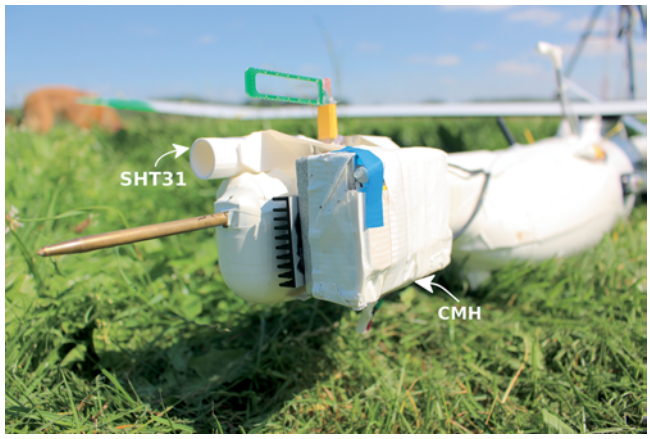

Figure 3: Sensor dome of the research UAS MASC-3 shortly before take-off, holding the five-hole probe (brass tube), CMH with radiator (white box with blue stripe) and SHT31 thermo- and hygrometer (inside the white radiation shield). The green bracket is holding a fine wire platinum resistance thermometer.

Table 2: System characteristics of the MASC-3 UAS at a usual measurement campaign.

wingspan	4 m
total weight	≈7 kg
sci. payload	≈1 kg
cruising speed	19 m s^{-1}
endurance	up to 2.5 h
propulsion	electrical pusher engine
take-off	bungee or winch

flight control, it uses a Pixhawk 2.1 "Cube" autopilot (Pixhawk-Organisation, 2019) to follow waypoints defined by the ground station operator at a constant airspeed typically around 18 m s^{-1}.

The MASC-3 system allows in-situ high-frequency measurements of the atmospheric flow (pressure) using a five-hole probe and air temperature using a fine wire platin resistance thermometer, thus it is able to resolve turbulent structures at very small scale (Mauz et al., 2019). All measured data is stored using a logging frequency of 500 Hz. After post-processing all data are scaled and available in 100 Hz. Additionally to atmospheric parameters the necessary GPS positioning and orientation angles and angular accelerations are logged by an IMU (inertial measurement unit). A detailed description of the UAS and its instrumentation can be found in Rautenberg et al. (2019). The chilled-mirror high-frequency humidity sensor has been implemented into the sensor system of the MASC-3 and can be post-processed in the same manner as all on-board sensors. The sensor weighs approximately 200 g and the hardware is in a 92 mm × 60 mm ×30 mm (L×W×H) box (cf. Figure 3).

3.2 Data for comparison and measurement site

In order to test and evaluate the system, a measurement flight took place at the WINSENT wind-energy test site at the Swabian Alb near the town of Donzdorf, Germany. The aim of the WINSENT project is to evaluate the local wind field, and to investigate orographical induced turbulence, and the stress it induces on wind energy converter blades, caused by the transition from a plateau to low lands by a steep escarpment of about 200 m height. The site is still in preparation, and two wind energy converters (WECs) will be installed until autumn 2020. At present, a 100 m tall meteorological tower (location 48.6652 N, 9.8348 E) is installed on the plateau, directly behind the forested escarpment. The tower (Figure 4) has a lateral distance of 80 m to the escarpment. On the tower, meteorological parameters are measured at several heights. To minimize the impact of the tower structure on the measurements for the predominant westerly as well as easterly winds, all sensors are installed on horizontal booms of 1 to 3 m length extending towards north and south.

The MASC-3 measurements are captured in so-called 'flight legs'. A leg is the straight and level section of a UAS flight pattern (see logged flight path in Figure 5).

The UAS captured data starting at 20 m a.g.l up to 140 m a.g.l in 20 m intervals and as well in 180 and 220 m a.g.l. At each altitude, four to six flight legs were flown. The pink 'x' in Figure 5 marks the location of the meteorological observation tower. For the tower comparison, only data in-between the blue planes in Figure 5 are used. The main wind direction is 100° with an average horizontal wind velocity of $v_h \approx 5\,\mathrm{m\,s^{-1}}$. The measurements took place on August 23rd, 2019, on a sunny day from 10:00 to 12:00 UTC (12:00 to 14:00 LT). During the flights the stratification of the atmosphere was slightly unstable and the surface temperature was 18.5 °C.

The in-house made high-response humidity sensor is compared against a capacitive humidity sensor (Sensirion SHT31) aboard MASC-3, as well as against several capacitive hygrometers mounted on the

Table 3: Sensors used in dew point comparison with CMH.

Location	Manufacturer	Measurand	Range	Accuracy	Meas. element	Response time
Tower	Thies	Temperature	−30…+70 °C	±0.1 K	Electr. resistance	$\tau_9 0 < 20$ s
Tower	Thies	Humidity	0…100 % r.H.	±2 % r.H.	Capacitive	$\tau_9 0 < 20$ s
MASC-3	Sensirion SHT31	Temperature	0…+90 °C	±0.2 K	Electr. resistance	$\tau_6 3 > 2$ s
MASC-3	Sensirion SHT31	Humidity	0…100 % r.H.	±2 % r.H.	Capacitive	$\tau_6 3 \approx 8$ s

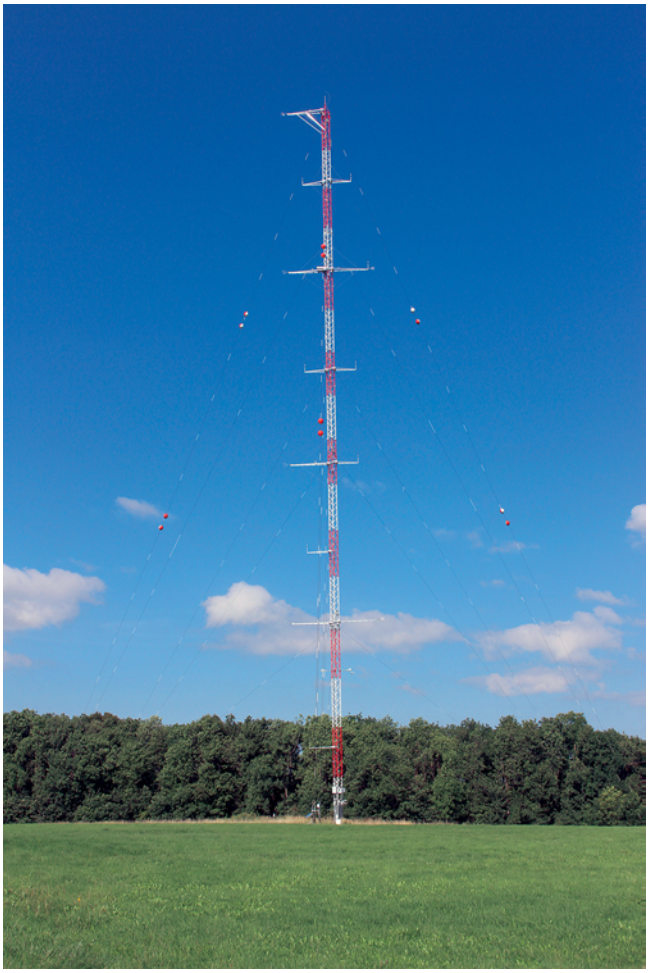

Figure 4: Meteorological 100 m measurement tower at the WINSENT test site on a plateau. Capacitive hygrometers are installed at different altitudes (23, 45, 73, 96 m a.g.l). The photograph is facing west. (Photo taken by the author).

meteorological tower (Figure 4). The tower sensors are Thies thermo- and hygrometers (model numbers 1.1005.54.34x) mounted at heights of 23 m, 45 m, 72 m and 96 m (see also Table 3 and Figure 5). All capacitive humidity sensors yield data at a low temporal resolution (1 Hz), which makes them suitable for comparison at low frequencies only. Leg averages of 130 m (approximately 700 data points) of the MASC-3 measurements directly in front of the met-tower are compared to temporal averages of the tower data using an equivalent fetch of about 4 min, which is the same time frame as the MASC-3 measurement took place.

3.3 Data conversion

The Thies thermo- and hygrometers and the SHT31 sensor both measure ambient temperature ϑ (°C) and relative humidity r (% r.H). To convert the relative humidity measurement (r) to dew point temperature (ϑ_d), the relation given in Eq. 3.1 and the Magnus formula Eq. 3.2 are used, giving the saturation pressure for water vapour (E) with r ranging from 0 to 1.

$$E(\vartheta_\mathrm{d}) = r \cdot E(\vartheta) \tag{3.1}$$

$$E(\vartheta) = E_0 \cdot \exp\left(\frac{a \cdot \vartheta}{b + \vartheta}\right), \tag{3.2}$$

with $E_0 = 6.111$ hPa, $a = 17.51$ and $b = 241.2$ °C

$$E(\vartheta_\mathrm{d}) = E_0 \cdot \exp\left(\frac{a \cdot \vartheta_\mathrm{d}}{b + \vartheta_\mathrm{d}}\right) = r \cdot E_0 \cdot \exp\left(\frac{a \cdot \vartheta}{b + \vartheta}\right) \tag{3.3}$$

Solving Eq. 3.3 for the dew point temperature ϑ_d yields Eq. 3.4. This equation can then be used to calculate the dew point directly from the relative humidity and ambient temperature measurement (Sonntag and Heinze, 1982).

$$\vartheta_\mathrm{d}(r, \vartheta) = \frac{b \cdot \ln(r) + \frac{a \cdot b \cdot \vartheta}{b+\vartheta}}{a - \ln(r) - \frac{a \cdot \vartheta}{b+\vartheta}} \tag{3.4}$$

4 Results

This section is divided into three subsections. In the first subsection exemplary spatial series of the CMH and SHT31 aboard MASC-3 are examined, as well as a short quality control is presented. Secondly, a low frequency response evaluation and a comparison of CMH measurements to tower measurements by averaged values is presented. Finally, the high frequency results (spectra, structure function) are presented.

4.1 Quality control and low frequency response

Figure 6 shows an exemplary spatial series of the high-response CMH and the capacitive SHT31 sensor mounted on the sensor dome (Figure 3) of the MASC-3 measured during a flyby at 120 m a.g.l. The spatial series shows that both sensors measured the same low-frequency changes in humidity, i.e. peak position and trend. The spatial series shows an expected dew point distribution in a well mixed layer near the surface. The

Figure 5: Top view of the measurement site from Google Earth. The pink 'x' marks the position of the met-tower near the town of Stötten. The N–S oriented flight path of the UAS is shown in yellow, tracked by the GPS system of the UAS, a green arrow indicates the easterly wind direction. For the tower comparison only data captured in-between the two blue planes is used. The measurements took place on August 23rd, 2019, on a sunny day from 10:00 to 12:00 UTC (12:00 to 14:00 LT).

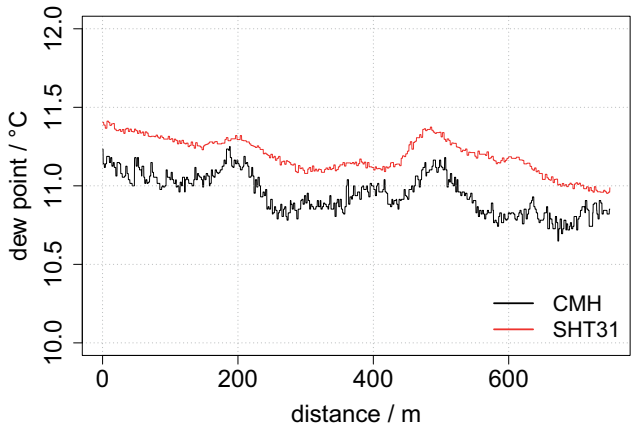

Figure 6: Spatial series along the whole distance of the measurement leg with the two sensors mounted onto the sensor dome of the MASC UAS. Both sensors measure the same signal. Noticeable is the constant offset between the two measurements. Also the SHT31 shows a distinct inertness (time constant of 8 s according to the manufacturer).

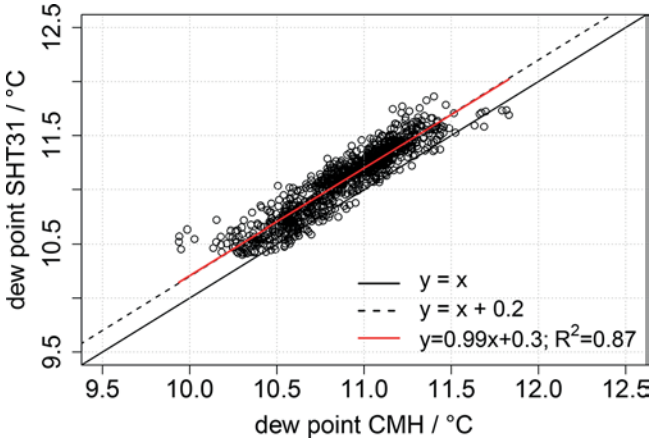

Figure 7: Scatter plot of all data obtained in 30 legs in various altitudes. The measurements are block averaged over 100 data points (1 s). The black solid line marks a 1:1 relationship, the black dashed line takes account of the constant offset between both sensors. The red solid line is the actual linear relationship of both sensors.

peaks are advected moisture by the piggery upstream. The correlation coefficient of both sensors for this measurement leg is 0.81. The high-response hygrometer shows more variations and resolves small-scale changes of the dew point temperature. It responses much faster than the SHT31, that has a response time τ_{63} of 8 s, according to the manufacturer at a flow velocity of 1 m s^{-1}. With τ_{63} the time that it takes for the sensor to measure 63 % of a signal at a change of input. Thus, the SHT31 signal shows a distinct inertness, compared to the CMH signal.

As mentioned in Section 2.2, the chilled-mirror hygrometer and the capacitive SHT31 sensor show a constant offset of ca. 0.2 K that is caused by setting the illumination target level criterion in the calibration.

For a more in depth evaluation of the measured data of the CMH and the SHT31 sensor, Figure 7 shows a scatter plot of all measurements taken in several flight legs over various altitudes. For the scatter plot evaluation, the data were block averaged over 100 data points (1 s). Both sensors show good correlation $R^2 = 0.87$ or $R = 0.93$, resulting in a good linear regression (red line) with a slope of $0.99 \approx 1$. In the scatter plot the dashed black line is taking account of the constant offset between both sensors of 0.2 K and almost superimposes with the linear regression.

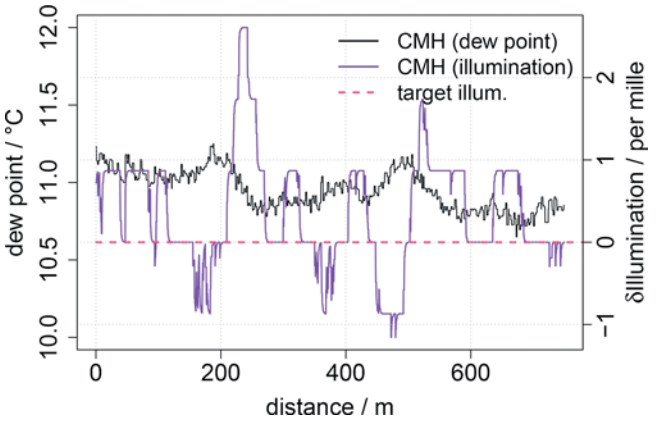

Figure 8: Spatial series of the CMH dew point temperature and the corresponding deviation of the illumination signal. The illumination fluctuates around 2 ‰ of its target value.

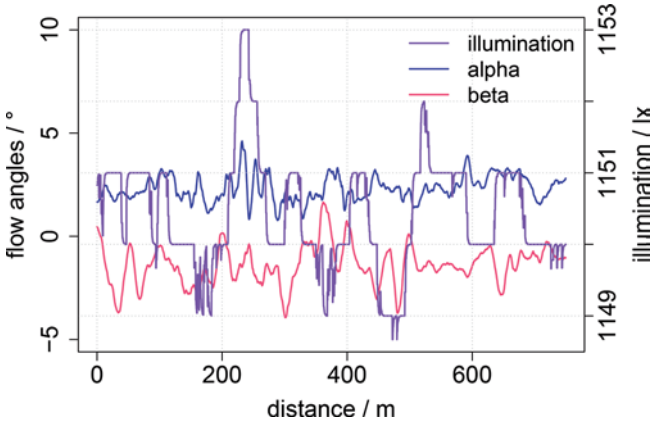

Figure 9: Flow angles alpha (angle of attack) and beta (side-slip) in degrees and absolute illumination at the TEC surface. A moving average over 50 data points (0.5 s) has been applied onto the time series of the flow angles.

In addition to the CMH spatial series, Figure 8 shows the measured deviation of the illumination signal (reflected light) of the CMH (purple line) from the target illumination (red dashed line). The illumination signal is the input parameter for the PID controller that regulates the voltage applied to the TEC. The maximum deviation in this exemplary measurement is approximately 2.5 ‰ from the target illumination (±3 lx at 1150 lx). A constant illumination is equatable to an equilibrium of evaporation (of condensed dew) and condensation (of water vapour). Thus, the mirror coating is held continuously at the mirror with only remaining insignificant variations. These are the variations that induce the PID regulation, but are kept down to a very minimum of ±3 lx.

To rule out that changes of the ram air affect the illumination, the measured flow angles (angle of attack and sideslip) for the exemplary flight leg in this study are calculated and shown in Figure 9. The angle of attack is the angle between the body's reference line (longitudinal axis through the fuselage of the UAS, i.e. back to front) and the oncoming flow in the vertical direction. The side-slip is the angle relating to the rotation of the aircraft centreline from the relative wind.

The blue and pink line are the angle of attack and side-slip of the airflow. The purple line is the measured illumination. The correlation coefficient between the illumination and alpha or beta equals 0.15 and −0.08 respectively. Note, that for this study, and for turbulence measurements in general, if a correlation is calculated in the order of $r \approx |0.2|$ to $|0.25|$ and it can be seen as a criterion of 'not correlated'. Hence, it can be concluded that at least for these angles, the CMH operates independently and is not affected by slight flow variations.

4.2 Comparison with tower data

Figure 10 shows averaged data of the available flight legs for each altitude. The offset between CMH (black) and SHT31 (red) is clearly visible. the tower measurements are seemingly systematically lower than the UAS measurements at low altitudes and systematically higher

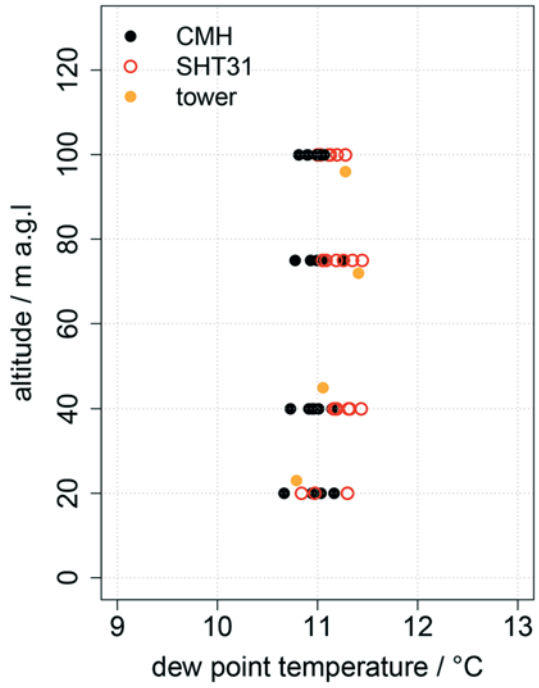

Figure 10: Measured dew point temperatures with a capacitive humidity sensor SHT31 and the CMH aboard the MASC-3 UAS. The measurements marked in orange are from capacitive hygrometers mounted on a meteorological tower about 50 m downstream.

at high altitudes, even if there is no clear explanation for that at the moment. It might be that the installation position on the met-tower influences the measurement, a calibration error or drifting of the capacitance sensor.

Each level shows six data points, with each point corresponding to the one of the six flight-leg's sections of ca. 130 m. The standard deviation for the measurements at each level is approximately 0.1 K. The orange circles (Figure 10) are the values obtained from the Thies hygrometers on the meteorological tower, which is located approximately 50 m downstream of the MASC-3 flight path. Averages of each tower level were obtained

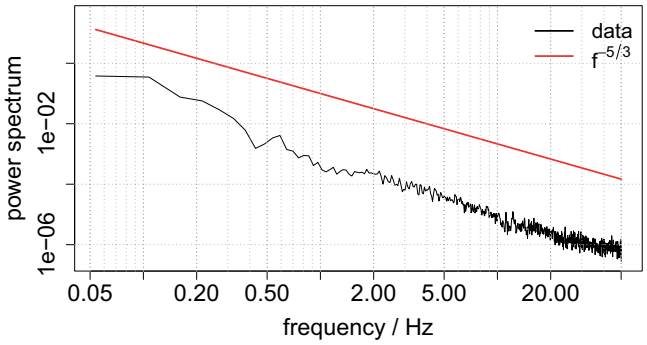

Figure 11: Frequency response (f) from an average power spectrum calculated from 14 measurement legs over the first four altitudes.

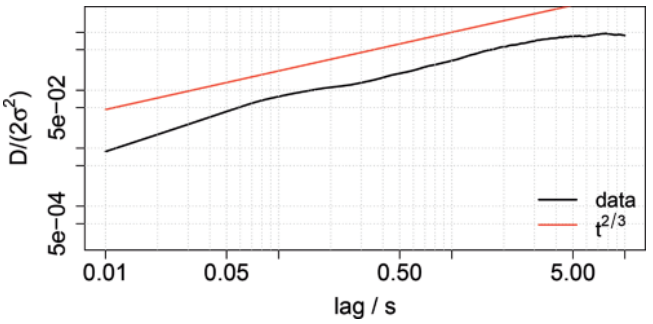

Figure 12: Exemplary structure function D of a measurement along a flight path in 120 m a.g.l in front of the meteorological tower. The red line is the reference lag$^{2/3}$.

over a time window of approximately 4 min during which the MASC-3 UAS measured at the corresponding altitude, i.e. one average over the whole duration of all six flight legs. For a horizontal wind speed of approximately 5 m s^{-1}, this window corresponds to a 1250 m fetch. Considering that the location of the tower sensors and MASC-3 flight-sections of each leg do not coincide, the averaged tower-based data is in good agreement ($\Delta K \approx 0.5$–$1\ K$) with the MASC measurements.

4.3 High frequency response

The main goal of developing a high-frequency humidity sensor for an unmanned airborne platform is to measure humidity fluctuations related to atmospheric turbulence. Consequently, the sensor requires a temporal resolution of at least 5–10 Hz to resolve eddies of 2 m size when measuring at an air speed of 20 m s^{-1}. For the high frequency analysis, power spectra of the CMH signal are evaluated. Figure 11 shows the average of 14 power spectra captured at the lowest four measurement altitudes (20, 30, 40 and 60 m a.g.l). The spectrum shows resolved turbulence in the inertial sub-range up to ca. 10 Hz, visible by the black curve following the Kolmogorov (1941) five-thirds law (red line). For higher frequencies a bend is visible.

As a second quality check of high-frequency response functionality, the structure function D of a single leg is calculated. The eddy-size distribution of a turbulent flow in the inertial sub-range, or the local structure of a turbulent flow, was first and foremost quantified using the (auto-) structure function (Kolmogorov, 1941), see also Bange (2009) and Wildmann et al. (2013).

$$D_{\phi(\tau)} = \frac{1}{D-\tau} \int_0^{D-\tau} dt\,[\phi(t+\tau) - \phi(t)]^2 \qquad (4.1)$$

where τ is the lag or shift, ϕ is the physical quantity, D is the total length of the time series and t is the time.

To simplify the interpretation of structure functions, they can be normalized by dividing by twice the variance of the corresponding time series:

$$\frac{D_\phi}{2\sigma^2} = \begin{cases} 0 & : \text{fully correlated} \\ 1 & : \text{non-correlated} \\ 2 & : \text{fully anti-correlated} \end{cases} \qquad (4.2)$$

Now, it is desired that the investigated data follows the $t^{2/3}$ line to the lowest lags possible, since the lowest point of parallelism is equal to the time constant of the sensor.

The structure function in Figure 12 shows a near parallel distribution to the Kolmogorov distribution (red line). Clear deviations from this line are observed for $\tau < 0.1$ s, or $1/\tau = 10$ Hz. This is in accordance with the characteristics observed in the averaged spectra presented in Figure 11. At the low frequency end the Kolmogorov inertial sub-range of locally isotropic turbulence is left at about 5 s. With an average flight velocity of 18 m s^{-1} this corresponds to eddies with diameters of 90 m, and might mark the beginning of the turbulent production range due to the relatively low flight altitude. The minor deviations from the 'ideal' Kolmogorov distribution between 0.1 s and 5 s could be explained by the heterogeneous inflow due to the complex terrain (escarpment, forests).

5 Conclusions and outlook

The first measurements of the in-house built high-frequency CMH aboard of an UAS type MASC-3 show good agreement compared to two industrial-made capacitive sensor types. One of the capacitive sensors is directly mounted next to the CMH and in good agreement with it (it shows the same peaks and trends). An offset of the CMH with respect to the capacitive sensor is related to the calibration that optimizes the sensor's data output. Due to the same mean variation of the CMH and the SHT31, we estimate an achieved accuracy of the CMH of ±0.2 K. For obvious reasons the hygrometers mounted on the meteorological observation tower do not measure identical values as the MASC-3 based

sensors. Nonetheless, the averages of the tower measurements are in good agreement with the UAS-based measurements. Considering the difficulty in comparing mobile line data to tower data, we find all sensors in good accordance (0.2 K off-set between both sensors aboard the UAS) to each other.

Concerning the high-frequency response of the CMH, it can be concluded that the CMH resolves the atmospheric dew point up to ≈ 10 Hz. Taking all measurements and the frequency response evaluation into account, the overall accuracy is promising. Measurements to compare the CMH sensor against absorption high-frequency instruments are planned. This will then allow for a comparison of turbulent latent heat fluxes. All measurements have been made along straight flight legs. The CMH is optimised for a constant air flow (constant TAS), regulated by the Pixhawk autopilot. Also changes in air flow are not critical as long as these changes occur slowly. It has been shown that the CMH sensor is not prone to small variations in flow angles (Figure 9).

The presented sensor has been assembled out of spare parts (TEC, mirror, TC). The signal processing is based on a microcontroller. In our first attempt an Arduino Nano has been chosen. A possible next step is using a more powerful microprocessor. This would increase the logging/processing frequency and therefore decrease the regulation intervals of the PID controller. A more precise and instant regulation of the TEC would then be possible. Another major improvement can be done by upgrading the temperature measurement. At the moment the TC read-out is one of the bottlenecks of the sensor.

Yet, a faster read-out of the temperature measurement does not equal a faster sensor. An important factor is also the thickness of the mirror, and TEC insulation. The thicker (and bigger) all these components are, the higher is the cumulative heat capacity that slows down heat transfer. An ideal TEC (or CMH) should have a heat capacity of zero, thus this is not possible, since all parts inherit mass. However, the cumulative heat capacity can be minimised by downsizing the TEC and mirror.

The next step is to improve the aerodynamics of the sensor. This contributes to the complete sensor system and handling of the aircraft. Also the inlet for the ram air will be reaching farther into the undisturbed air, to minimise the impact of the fuselage and its boundary layer.

In this study the presented prototype was equipped on an UAS. It is also possible to use the CMH system in eddy covariance (EC) stations once the sensor is ventilated properly. The CMH can also be used in still air, as long as the heat sink is cooled down properly. It is also possible to tune the PID controller to other wind/flow conditions than in the present case.

The CMH can also be calibrated against an absorption hygrometer (e.g. IRGASON, a combined gas analyser and sonic anemometer) to determine the absolute accuracy of the sensor. At the time of the study, no such high accuracy hygrometer was available.

Acknowledgements

We acknowledge support by the Projektträger Jülich (PtJ) for the WINSENT test site (project grant number: 0324129D) funded by the BMWi (German Federal Ministry for Economic Affairs and Energy). We also thank the Zentrum für Sonnenenergie und Wasserstoff-Forschung Baden-Württemberg (ZSW) for providing the tower measurement data. For technical support we thank Claudio Crazzolara, Hasan Mashni and Henrik Rieth.

We also acknowledge support by Open Access Publishing Fund of University of Tübingen.

References

Baldocchi, D., E. Falge, L. Gu, R. Olson, D. Hollinger, S. Running, P. Anthoni, C. Bernhofer, K. Davis, R. Evans, J. Fuentes, A. Goldstein, G. Katul, B. Law, X. Lee, Y. Malhi, T. Meyers, W. Munger, W. Oechel, K.T. Paw U, K. Pilegaard, H.P. Schmid, R. Valentini, S. Verma, T. Vesala, K. Wilson, S. Wofsy, 2001: Fluxnet: A new tool to study the temporal and spatial variability of ecosystem-scale carbon dioxide, water vapor, and energy flux densities. – Bull. Amer. Meteor. Soc. **82**, 2415–2434.

Bange, J., 2009: Airborne Measurement of Turbulent Energy Exchange Between the Earth Surface and the Atmosphere. – Sierke Verlag, Göttingen.

Bange, J., R. Roth, 1999: Helicopter-borne flux measurements in the nocturnal boundary layer over land – a case study. – Bound.-Layer Meteor. **92**, 295–325, DOI: 10.1023/A:1002078712313.

Beyrich, F., S.H. Richter, U. Weisensee, W. Kohsiek, H. Lohse, de H.A.R. Bruin, T. Foken, M. Göckede, F. Berger, R. Vogt, E. Batchvarova, 2002a: Experimental determination of turbulent fluxes over the heterogeneous litfass area: Selected results from the litfass-98 experiment. – Theor. Appl. Climatol. **73**, 19–34, DOI: 10.1007/s00704-002-0691-7.

Beyrich, F., H.J. Herzog, J. Neisser, 2002b: The litfass project of dwd and the litfass-98 experiment: The project strategy and the experimental setup. – Theor. Appl. Climatol. **73**, 3–18, DOI: 10.1007/s00704-002-0690-8.

Beyrich, F., J.P. Leps, M. Mauder, J. Bange, T. Foken, S. Huneke, H. Lohse, A. Lüdi, W.M.L. Meijninger, D. Mironov, U. Weisensee, P. Zittel, 2006: Area-averaged surface fluxes over the litfass region based on eddy-covariance measurements. – Bound.-Layer Meteor. **121**, 33–65, DOI: 10.1007/s10546-006-9052-x.

Bogena, H.R., R. Bol, N. Borchard, N. Brüggemann, B. Diekkrüger, C. Drüe, J. Groh, N. Gottselig, J.A. Huisman, A. Lücke, A. Missong, B. Neuwirth, T. Pütz, M. Schmidt, M. Stockinger, W. Tappe, L. Weihermüller, I. Wiekenkamp, H. Vereecken, 2015: A terrestrial observatory approach to the integrated investigation of the effects of deforestation on water, energy, and matter fluxes. – Sci. China Earth Sci. **58**, 61–75, DOI: 10.1007/s11430-014-4911-7.

De Bruin, H.A.R., W. Kohsiek, B.J.J.M. Van Den Hurk, 1993: A verification of some methods to determine the fluxes of momentum, sensible heat, and water vapour using standard deviation and structure parameter of scalar meteorological quantities. – Bound.-Layer Meteor. **63**, 231–257, DOI: 10.1007/BF00710461.

Foken, T., 2008: The energy balance closure problem: an overview. – Ecolog. Appl. **18**, 1351–1367, DOI: 10.1890/06-0922.1.

Fujiwara, M., M. Shiotani, F. Hasebe, H. Vömel, S.J. Oltmans, P.W. Ruppert, T. Horinouchi, T. Tsuda, 2003: Performance of the meteolabor "snow white" chilled-mirror hygrometer in the tropical troposphere: Comparisons with the vaisala rs80 a/h-humicap sensors. – J. Atmos. Ocean. Technol. **20**, 1534–1542, DOI: 10.1175/1520-0426(2003)020<1534:POTMSW>2.0.CO;2.

Kolmogorov, A.N., 1941: The Local Structure of Turbulence in Incompressible Viscous Fluid for Very Large Reynolds' Numbers. – In: Dokl. Akad. Nauk SSSR, Volume **30**, 301–305.

Koufang Lo, A., 1996: The importance of humidity effect in determining flux-profile parameters of a marine surface layer. – J. Appl. Meteor. **35**, 978–986, DOI: 10.1175/1520-0450(1996)035<0978:TIOHEI>2.0.CO;2.

Kuner, R., S. Rudersdorf, O. Schulze, 2015: Vorschriften und Betriebsunterlagen Nr. 3: Technikhandbuch für Wettermeldestellen des synoptisch-klimatologischen Mess- und Beobachtungsnetzes. – Technikhandbuch, Deutscher Wetterdienst, Offenbach.

Lampert, A., J. Hartmann, F. Pätzold, L. Lobitz, P. Hecker, K. Kohnert, E. Larmanou, A. Serafimovich, T. Sachs, 2018: Comparison of lyman-alpha and li-cor infrared hygrometers for airborne measurement of turbulent fluctuations of water vapour. – Atmos. Measur. Techn. **11**, 2523–2536, DOI: 10.5194/amt-11-2523-2018.

Mammarella, I., S. Launiainen, T. Gronholm, P. Keronen, J. Pumpanen, U. Rannik, T. Vesala, 2009: Relative humidity effect on the high-frequency attenuation of water vapor flux measured by a closed-path eddy covariance system. – J. Atmos. Ocean. Technol. **26**, 1856–1866, DOI: 10.1175/2009JTECHA1179.1.

Mauz, M., A. Rautenberg, A. Platis, M. Cormier, J. Bange, 2019: First identification and quantification of detached-tip vortices behind a wind energy converter using fixed-wing unmanned aircraft system. – Wind Energy Sci. **4**, 451–463, DOI: 10.5194/wes-4-451-2019.

Meijninger, W.M.L., F. Beyrich, A. Lüdi, W. Kohsiek, H.A.R. De Bruin, 2006: Scintillometer-based turbulent fluxes of sensible and latent heat over a heterogeneous land surface – a contribution to litfass-2003. – Bound.-Layer Meteor. **121**, 89–110, DOI: 10.1007/s10546-005-9022-8.

Metzger, S., W. Junkermann, B.B. K, H. Schmid, T. Foken, 2011: Measuring the 3-d wind vector with a weight-shift microlight aircraft. – Atmos. Meas. Tech. **4**, DOI: 10.5194/amtd-4-1303-2011.

Muschinski, A., R. Frehich, M. Jensen, R. Hugo, A. Hoff, F. Eaton, B. Balsley, 2001: Fine-scale measurements of turbulence in the lower troposphere: An intercomparison between a kite- and balloon-borne, and a helicopter-borne measurement system. – Bound.-Layer Meteor. **98**, 219–250, DOI: 10.1023/A:1026520618624.

Narvekar, S.V., V.K. Upadhye, 2016: Review of PI and PID controllers. – Int. J. Recent Trends Engineer. Res. **2**, 381–387.

Neininger, B., J. Hacker, 2012: Manned or unmanned – does this really matter?. – International Archives of the Photogrammetry, Remote Sensing and Spatial Information Sciences – ISPRS Archives **38**, 223–228, DOI: 10.5194/isprsarchives-XXXVIII-1-C22-223-2011.

neonscience.org, 2019: National science foundation's national ecological observatory network (NEON). – https://www.neonscience.org/data-collection/flux-tower-measurements (accessed: 2019-11-04).

Pixhawk-Organisation, 2019: Pixhawk 2.1 autopilot description. – http://pixhawk.org (accessed: 2019-07-01).

Platis, A., A.F. Moene, D.M. Villagrasa, F. Beyrich, D. Tupman, J. Bange, 2017: Observations of the temperature and humidity structure parameter over heterogeneous terrain by airborne measurements during the litfass-2003 campaign. – Bound.-Layer Meteor. **165**, 447–473, DOI: 10.1007/s10546-017-0290-x.

Rao, K.R., R. Mishra, 2014: Comparative Study of P, PI and PID Controller for Speed Control of VSI-fed Induction Motor. – Int. J. Engin. Develop. Res. **2**, 16512031.

Rautenberg, A., M. Schön, zum K. Berge, M. Mauz, P. Manz, A. Platis, van B. Kesteren, I. Suomi, S.T. Kral, J. Bange, 2019: The multi-purpose airborne sensor carrier masc-3 for wind and turbulence measurements in the atmospheric boundary layer. – Sensors **19**, 2292, DOI: 10.3390/s19102292.

Rebmann, C., M. Aubinet, H. Schmid, N. Arriga, M. Aurela, G. Burba, R. Clement, A. De Ligne, G. Fratini, B. Gielen, J. Grace, A. Graf, P. Gross, S. Haapanala, M. Herbst, L. Hörtnagl, A. Ibrom, L. Joly, N. Kljun, O. Kolle, A. Kowalski, A. Lindroth, D. Loustau, I. Mammarella, M. Mauder, L. Merbold, S. Metzger, M. Mölder, L. Montagnani, D. Papale, M. Pavelka, M. Peichl, M. Roland, P. Serrano-Ortiz, L. Siebicke, R. Steinbrecher, J.P. Tuovinen, T. Vesala, G. Wohlfahrt, D. Franz, 2018: ICOS eddy covariance flux-station site setup: a review. – Int. Agrophys. **32**, 471–494, DOI: 10.1515/intag-2017-0044.

Shuttleworth, W., 2007: Putting the "vap" into evaporation. – Hydrol. Earth Sys. Sci. **11**, 210–244, DOI: 10.5194/hess-11-210-2007.

Sonntag, D., D. Heinze, 1982: Sättigungsdampfdruck- und Sättigungsdampfdichtetafeln für Wasser und Eis (1. Aufl.). – Deutscher Verlag für Grundstoffindustrie, Leipzig.

Spiess, T., J. Bange, M. Buschmann, P. Vörsmann, 2007: First application of the meteorological Mini-UAV 'M2AV'. – Meteorol. Z. **16**, 159–169, DOI: 10.1127/0941-2948/2007/0195.

Stull, R., 2000: Meteorology for Scientists and Engineers. – Brooks/Cole, Belmond CA, USA.

van den Kroonenberg, A.C., S. Martin, F. Beyrich, J. Bange, 2012: Spatially-averaged temperature structure parameter over a heterogeneous surface measured by an unmanned aerial vehicle. – Bound.-Layer Meteor. **142**, 55–77, DOI: 10.1007/s10546-011-9662-9.

Van Kesteren, B., O.K. Hartogensis, D. Van Dinther, A.F. Moene, H.A.R. De Bruin, 2013a: Measuring H2O and CO2 fluxes at field scales with scintillometry: Part i – introduction and validation of four methods. – Agricult. Forest Meteor. **178-179**, 75–87, DOI: 10.1016/j.agrformet.2012.09.013.

Van Kesteren, B., O.K. Hartogensis, D. Van Dinther, A.F. Moene, H.A.R. De Bruin, A.A.M. Holtslag, 2013b: Measuring H2O and CO2 fluxes at field scales with scintillometry: Part ii – validation and application of 1-min flux estimates. – Agricult. Forest Meteor. **178-179**, 88–105, DOI: 10.1016/j.agrformet.2013.01.010.

Vömel, H., M. Fujiwara, M. Shiotani, F. Hasebe, S. Oltmans, J. Barnes, 2003: The behavior of the snow white chilled-mirror hygrometer in extremely dry conditions. – J. Atmos.Ocean. Technol. **20**, 1560–1567, DOI: 10.1175/1520-0426(2003)020<1560:TBOTSW>2.0.CO;2.

Ward, H.C., J.G. Evans, C.S.B. Grimmond, J. Bradford, 2015a: Infrared and millimetre-wave scintillometry in the suburban environment – Part 1: Structure parameters. – Atmos. Measur. Techn. **8**, 1385–1405, DOI: 10.5194/amt-8-1385-2015.

Ward, H.C., J.G. Evans, C.S.B. Grimmond, 2015b: Infrared and millimetre-wave scintillometry in the suburban environment – Part 2: Large-area sensible and latent heat

fluxes. – Atmos. Measur. Techn. **8**, 1407–1424, DOI: 10.5194/amt-8-1407-2015.

Wildmann, N., M. Mauz, J. Bange, 2013: Two fast temperature sensors for probing of the atmospheric boundary layer using small Remotely Piloted Aircraft (RPA). – Atmos. Measur. Techn. **6**, 2101–2113, DOI: 10.5194/amt-6-2101-2013.

Wildmann, N., F. Kaufmann, J. Bange, 2014a: An inverse-modelling approach for frequency response correction of capacitive humidity sensors in abl research with small Remotely Piloted Aircraft (RPA). – Atmos. Measur. Techn. **7**, 3059–3069, DOI: 10.5194/amt-7-3059-2014.

Wildmann, N., M. Hofsäss, F. Weimer, A. Joos, J. Bange, 2014b: MASC; a small Remotely Piloted Aircraft (RPA) for wind energy research. – Adv. Sci. Res. **11**, 55–61, DOI: 10.5194/asr-11-55-2014.

Wildmann, N., S. Ravi, J. Bange, 2014c: Towards higher accuracy and better frequency response with standard multi-hole probes in turbulence measurement with remotely piloted aircraft (RPA). – Atmos. Measur. Techn. **7**, 1027–1041, DOI: 10.5194/amt-7-1027-2014.

Wolf, B., C. Chwala, B. Fersch, J. Garvelmann, W. Junkermann, M.J. Zeeman, A. Angerer, B. Adler, C. Beck, C. Brosy, P. Brugger, S. Emeis, M. Dannenmann, F. De Roo, E. Diaz-Pines, E. Haas, M. Hagen, I. Hajnsek, J. Jacobeit, T. Jagdhuber, N. Kalthoff, R. Kiese, H. Kunstmann, O. Kosak, R. Krieg, C. Malchow, M. Mauder, R. Merz, C. Notarnicola, A. Philipp, W. Reif, S. Reineke, T. Rödiger, N. Ruehr, K. Schäfer, M. Schrön, A. Senatore, H. Shupe, I. Völksch, C. Wanninger, S. Zacharias, H.P. Schmid, 2017: The scalex campaign: Scale-crossing land surface and boundary layer processes in the tereno-prealpine observatory. – Bull. Amer. Meteor. Soc. **98**, 1217–1234, DOI: 10.1175/BAMS-D-15-00277.1.